UC Irvine
UC Irvine Previously Published Works

Title

In-vivo 3D corneal elasticity using air-coupled ultrasound optical coherence elastography.

Permalink

Authors

Jin, Zi
Khazaeinezhad, Reza
Zhu, Jiang
et al.

Peer reviewed

In-vivo 3D corneal elasticity using air-coupled ultrasound optical coherence elastography

ZI JIN,[1,2,4] REZA KHAZAEINEZHAD,[1,4] JIANG ZHU,[1] JUNXIAO YU,[1] YUEQIAO QU,[1] YOUMIN HE,[1] YAN LI,[1] TOMAS E. GOMEZ ALVAREZ-ARENAS,[3] FAN LU,[2,5] AND ZHONGPING CHEN[1,6]

[1]*Beckman Laser Institute, Department of Biomedical Engineering, University of California, Irvine, Irvine, California 92612, USA*
[2]*School of Ophthalmology and Optometry, Wenzhou Medical University, Wenzhou 325003, Zhejiang, China*
[3]*Institute of Physical and Information Technologies, Spanish National Research Council (CSIC), 28006 Madrid, Spain*
[4]*These authors contributed equally to this work*
[5]*lufan62@mail.eye.ac.cn*
[6]*z2chen@uci.edu*

Abstract: Corneal elasticity can resist elastic deformations under intraocular pressure to maintain normal corneal shape, which has a great influence on corneal refractive function. Elastography can measure tissue elasticity and provide a powerful tool for clinical diagnosis. Air-coupled ultrasound optical coherence elastography (OCE) has been used in the quantification of ex-vivo corneal elasticity. However, in-vivo imaging of the cornea remains a challenge. The 3D air-coupled ultrasound OCE with an axial motion artifacts correction algorithm was developed to distinguish the in-vivo cornea vibration from the axial eye motion in anesthetized rabbits and visualize the elastic wave propagation clearly. The elastic wave group velocity of in-vivo rabbit cornea was measured to be 5.96 ± 0.55 m/s, which agrees with other studies. The results show the potential of 3D air-coupled ultrasound OCE with an axial motion artifacts correction algorithm for quantitative in-vivo assessment of corneal elasticity.

1. Introduction

The cornea, a transparent avascular connective tissue, is the principal refractive element in the eye due to its shape [1]. Cornea stiffness, also called corneal elasticity, can resist elastic deformations under intraocular pressure (IOP) to maintain normal corneal shape [2]. Several corneal diseases, such as corneal ectatic disorders, are assumed to be caused by the primary abnormalities of corneal stiffness [3]. As such, paying close attention to corneal stiffness may improve early diagnosis of corneal ectasia. Corneal refractive surgical techniques modify the curvature of the cornea to compensate for refractive errors. At the same time, they also alter the corneal stiffness, which may lead to post-refractive corneal ectasia [4]. Thus, it's suggested that a combination of residual stromal bed thickness with corneal stiffness can be used as a guide for corneal refractive surgery [5]. As an effective treatment for corneal ectatic disorders, corneal crosslinking (CXL) utilizes the chemical reaction of riboflavin and UV-A light to form new molecular bonds among corneal collagen fibrils to increase corneal stiffness [6,7]. Postoperative corneal stiffness is an important index to evaluate the stability of CXL [8]. Moreover, the measurement of IOP in clinical practice is indirect, and it should take the corneal stiffness with individual differences into consideration [9]. It's essential to evaluate the corneal stiffness accurately for compensation of IOP especially after refractive surgery [10] because accurate measurement of IOP is critical for glaucoma management [11].

Elastography is an in-vivo technique to assess the elasticity of biological tissue [12–14]. The principle of elastography is to deform the biological tissue using excitation mechanisms and

detect corresponding displacement responses by which the elasticity can be estimated [12,13]. Therefore, the elastography technique mainly consists of an excitation mechanism and an imaging system. Combining multiple excitation mechanisms with numerous imaging systems can develop different elastography techniques.

Among these elastography techniques, the ocular response analyzer (ORA) and the CorVis are two commercial devices currently available for clinical evaluation of corneal stiffness [15]. Both of them apply a large amplitude of air pulse to induce corneal displacement. However, the displacement induced by these two commercial devices is too large to measure corneal stiffness accurately due to a significant nonlinear component. In addition, the deformation amplitude of the cornea is affected by the stability of the air puff source, which only allows measurement of the relative elasticity [16]. When a tissue surface is excited by an excitation mechanism, an elastic wave is launched within the tissue [16]. It has been proven that the elastic wave velocity depends on the mechanical properties of tissues rather than the excitation mechanism and can be used to probe tissue elasticity in most studies [17–19].

It's thought that the cornea exhibits linear elasticity under small displacement (0.1%) [20]. Optical coherence elastography (OCE), based on optical coherence tomography (OCT) with high spatial and temporal resolutions, can detect micrometer-scale deformation [13]. Using the phase-resolved method, the resolution of the displacement measurement can be improved to subnanometer level [21,22]. For clinical application, a non-contact excitation mechanism, such as an air-puff or laser light, is necessary [16]. Air-puff OCE was first demonstrated to produce the elastic waves and measure in-vivo corneal elasticity [23,24]. But the repetition of the air-puff is limited to about 100 Hz which restricts the sampling rate of the imaging technique, especially in 3D imaging [13,25]. Although a high pulse laser can be used to induce displacement, the required energy of the laser exceeds the safety limits [17]. Recently, a non-contact, high repetition, and safe air-coupled ultrasound technique emerged which makes it the ideal excitation mechanism for in-vivo corneal elastography [17,26].

OCE using air-coupled ultrasound as an excitation mechanism has been reported to map the 3D elasticity of porcine cornea ex-vivo [17]. However, this method has not been reported to measure corneal elasticity in-vivo. Compared with ex-vivo measurement, in-vivo measurement should take the effect of eye movement into account, especially when induced displacement is small [27].

In this study, we developed an OCE system based on air-coupled ultrasound excitation to provide quantitative assessment of elasticity in both phantom and corneal tissue. We report on the first in-vivo OCE imaging and quantification of corneas in an anesthetized rabbit based on an air-coupled ultrasound OCE system. An axial motion artifacts correction algorithm was also developed to extract the corneal vibration from Doppler phase images.

2. Materials and methods

2.1. Experimental setup

As shown in Fig. 1, the OCE system consists of a phase-resolved OCT and air-coupled ultrasound system. The phase-resolved OCT system using the sweep source laser (Axsun Technologies, Massachusetts, USA) with a center wavelength of 1310 nm and a scan repetition rate of 50 kHz is described in detail in our previous work [14,28]. A fiber Bragg grating (FBG) was added for triggering the A-scan acquisition to stabilize the phase in OCT data [29]. The phase stability of the system was experimentally measured to be ~2.8 mrad, thus yielding ~0.3 nm sensitivity in terms of displacement in the air. The air-coupled ultrasound system included a home-made focused air-coupled ultrasound transducer, power amplifier, and function generator. The employed air-coupled ultrasound transducer in this work has been specially designed to combine efficiency, focused field and relatively large bandwidth [30–33]. Transducer aperture was 25 mm and center frequency was 0.25 MHz with a 6 dB relative bandwidth of 57% and electrical impedance of

300 Ω (transmission mode). Transducer aluminum housing was ground connected to provide an effective electromagnetic shield. The two way insertion loss (i.e. transmission and reception together) was extremely low: −17 dB. The focalization was achieved by a quasi-spherical lens to keep both optimum focal spot and transducer efficiency. Focal distance was 65 mm, and 6dB size of the focal spot was 10 mm (axial) and 4 mm (transversal). The air-coupled ultrasonic transducer was driven by a burst signal of the sine wave amplified by the power amplifier. In order to induce the elastic wave, the air-coupled ultrasound transducer was tilted to the sample normal by about 45 degrees to avoid blocking the OCT beam. The scan protocol and synchronization of the transducer was controlled by an analog output device. The phase-resolved OCT system started to take data 2 ms before ultrasound excitation. Using an M-B scan mode, the elastic wave propagation was tracked for each B-scan slice: in the M-B scan, each M-scan consisted of 600 A-scans and 100 M-scans along lateral positions. For 3D OCE imaging, 20 different B-scan slices were framed to map the 3D elastic wave. Different concentration homogeneous agar phantoms and rabbit corneas in-vivo were imaged for three times to validate the method.
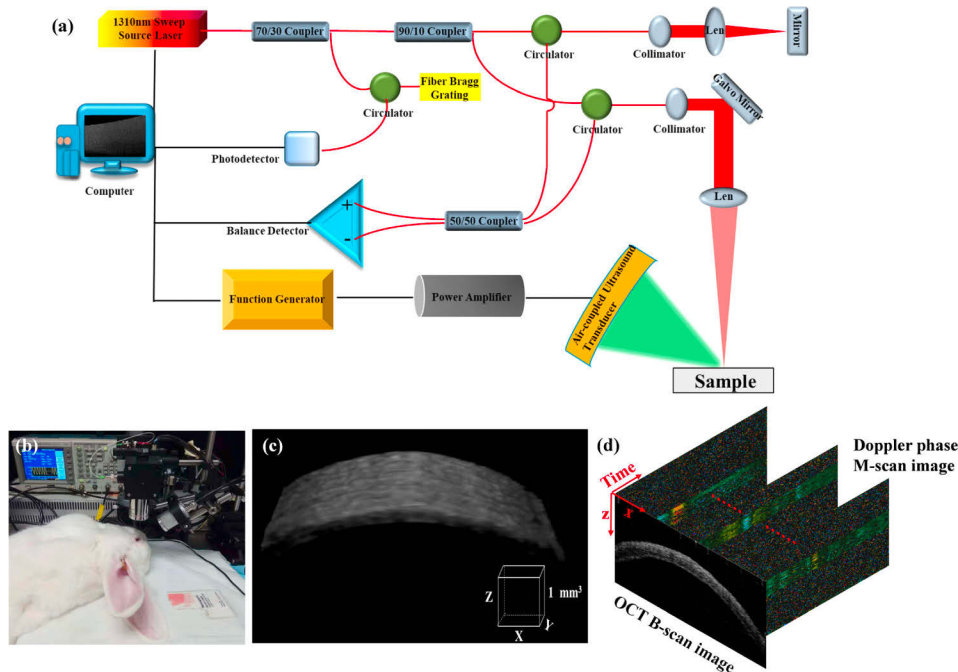
Fig. 1. System setup for in-vivo studies. (a) Schematic diagram of system. (b) Photo of the setup with the rabbit eye on the stage. (c) 3D OCT image of cornea in-vivo. (d) OCT M-B scan images of cornea in-vivo.

2.2. Material preparation

Two homogeneous agar phantoms with 0.3% (w/v), 0.7% (w/v) agar were made. For construction of a phantom, the granulated agar (Becton Dickinson Microbiology Systems Cockeysville, Maryland, USA) was dissolved in distilled water at 25 °C. Then the agar solution was stirred and heated until it boiled. After cessation of heating, the agar solution was cooled naturally to 60 °C with continuous stirring, and then 0.6% v/v intralipid solution was mixed with the agar solution for increase of backscattered signals. After stirring for 5 min, the final solution was poured into a cylindrical bottle with a top diameter of 17 mm and height of 56 mm to simulate the corneal diameter and stored in the refrigerator at 4 °C for solidification. In phantom experiments, the

transducer excitation parameters were set as follows: the voltage amplitude was 185 V, and the burst signal cycle number was 100. The scan range of the fast and slow scan directions were 10.94 mm and 3.75 mm, respectively. The excitation spot of the transducer was located at ~2 mm to the left of the scan area in the phantoms.

All rabbit experiments were performed with adherence to the guidelines set forth by the University of California, Irvine Institutional Animal Care and Use Committee (IACUC). Two healthy rabbits (a total of four eyes), weighting 4.58 kg and 4.68 kg, respectively, were imaged. Before imaging, general anesthesia was induced by subcutaneous injection of ketamine hydrochloride (35mg/kg) and xylazine hydrochloride (5 mg/kg). After general anesthesia, two drops of proparacaine hydrochloride were applied topically to provide additional local anesthesia. Normal saline solution was applied when the cornea dried. The rabbits were placed on the imaging stage and wore a pulse oximeter (Ohmeda Biox 3700 Pulse Oximeter, Pacific Medical, San Clemente, USA) to monitor the heart rate and oxygen saturation levels when they became unconscious. In the experiment, additional anesthesia via subcutaneous injection of 17.5 mg/kg ketamine was added every 30 min. After imaging, the rabbits were given buprenorphine for pain management, as necessary, and were monitored closely until they became fully conscious. Since corneal stiffness is larger than agar phantoms, it's necessary to optimize the transducer excitation parameters and scan protocol. The transducer was driven with the 234 v voltage amplitude and the 200 burst signal cycle number. And the scan range of the fast and slow directions were 7.72 mm and 3.75 mm, respectively. The excitation spot of the transducer was located at ~3.5 mm to the left of the scan area in the corneas.

2.3. Motion artifacts correction algorithm

Eye motion can be divided into transverse and axial according to the direction of motion in the scan coordinate system. The transverse eye motion is mainly caused by extraocular muscle movement while the axial eye motion is mainly caused by heartbeat and respiration [34]. However, involuntary saccades occur in the lateral directions even in rabbits anesthesized with ketamine/xylazine [35]. The Doppler phase shift used in this study is sensitive to axial motion, but not to lateral motion. Since lateral motion does not affect Doppler phase shift, it was negligible in this study. The axial eye motion is dependent on the pulse frequency and respiration rate of anesthetized rabbits which are 140-160/min, and 15-25/min, respectively.

The Doppler phase shift $\Delta\varphi(z)$ was calculated by the following equation in this study:

$$\Delta\phi(z) = \tan^{-1}\left(\frac{\text{Im}[\sum\limits_{z_m=z}^{z+M}\sum\limits_{j=1}^{N} I_j(z_m)\,\widetilde{I}_{j+Delay}(z_m)]}{\text{Re}[\sum\limits_{z_m=z}^{z+M}\sum\limits_{j=1}^{N} I_j(z_m)\,\widetilde{I}_{j+Delay}(z_m)]}\right) \tag{1}$$

where $I_j(z_m)$ are the complex signals at axial depth z_m corresponding to the j'th A-scan, $\widetilde{I}_{j+Dealy}(z_m)$ are the conjugate complex signals at axial depth z_m corresponding to the *Delay* A-scan adjacent to the j'th A-scan, M is an even number that denotes the window size in the axial direction for each pixel, and N is the number of sequential scans used to calculate the cross correlation. In this study, the M, N and *Delay* set 4, 4 and 20 to increase the signal-to-noise ratio of Doppler phase images.

In this study, a consecutive data correlation algorithm was used to correct the axial motion artifacts because the imaged object is inherently smooth and densely sampled by the OCT scan pattern [36]. Suppose the Doppler phase image (Fig. 2) obtained from the corneas is I_0 *(F, t)*, the true signal of interest is $I_{elastic}(F,\ t)$, and the axial eye motion is $I_{eye}(F,\ t)$, then the following formula can be derived:

$$I_0(F,\ t) = I_{elastic}(F,\ t) + I_{eye}(F,\ t) \tag{2}$$

where F is the sequence number of B-scan slices, and t is the time at which the phase image is located.
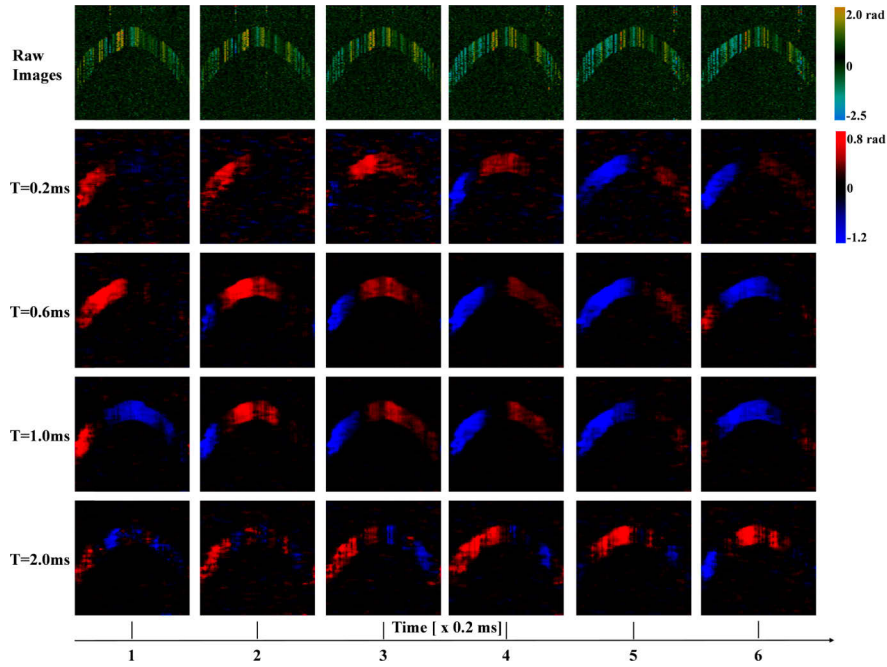
Fig. 2. Doppler phase images of the cornea before and after axial motion artifacts correction using different T values. The left column, except for the first row, represents the value of T. The sampling interval between images is 0.2 ms.

Since eye motion requires time to pass, it's thought that the eye is fixed during short time T. The variable $\Delta I_0(F, t)$ was calculated by the difference between the Doppler phase images with a time interval T to correct the eye motion (Fig. 2):

$$\Delta I_0(F, t) = I_0(F, t) - I_0(F, t + T). \tag{3}$$

Substitute Eq. (2) into Eq. (3) to get the following formula:

$$\Delta I_0(F, t) = I_{elastic}(F, t) + I_{eye}(F, t) - I_{elastic}(F, t + T) - I_{eye}(F, t + T). \tag{4}$$

Considering the relative stillness of the eye during time interval T, it is suggested

$$I_{eye}(F, t) - I_{eye}(F, t + T) = 0. \tag{5}$$

Thus, Eq. (4) can be simplified:

$$\Delta I_0(F, t) = I_{elastic}(F, t) - I_{elastic}(F, t + T). \tag{6}$$

It's very important to determine the value of T. Based on the elastic wave velocity and wavelength of rabbit corneas, the range of T value can be calculated roughly. As shown in Fig. 2, a different T value within its range was selected to correct the axial motion artifacts. The T value was optimized according to the signal-to-noise ratios (SNR) of Doppler phase images after correction. It's found if T is too small, the true signal of interest $I_{elastic}$ *(F, t)* will be offset; if T is too large, however, the eye motion can't be corrected completely. Therefore, T set 0.6 ms was a relatively good value for all rabbits in this study, and it can obtain high SNR of Doppler phase images after correction.

2.4. Elastic wave velocity measurement

Conventional transverse elastic wave velocity measurement is based on 2D Doppler phase images which measure the velocity along the fast scan direction [18,19,26,37]. However, when the measurement direction is not aligned with the elastic wave propagation direction, the calculated elastic wave velocity will be biased [38]. Therefore, it's necessary to measure the transverse elastic wave velocity along the fast and slow scan directions, respectively, so that the true transverse elastic wave velocity can be calculated precisely.

Suppose the velocity of the transverse elastic wave along the fast direction is V_x, and from the slow direction is V_y. The true transverse elastic wave velocity $V_{elastic}$ is expressed as follows [38]:

$$V_{elastic} = \frac{V_x V_y}{\sqrt{V_x^2 + V_y^2}}. \tag{7}$$

The complex boundary condition of corneas makes it difficult to obtain the elasticity modulus directly from the elastic wave velocity [16]. Since the thickness of the cornea is close to the order of the elastic wavelength and the boundary media are different on both sides, simple models such as the shear wave equation and Rayleigh wave equation are not suitable for the cornea [16]. A modified Rayleigh–Lamb frequency equation (mRLFE) that utilizes elastic wave phase velocities over a range of angular frequencies to quantify the corneal viscoelasticity has been reported [39,40]. The mRLFE yields a 5×5 matrix characteristic equation whose determinant is zero and can be solved only numerically according to the boundary conditions. It's found that the phase velocity of Lamb waves in the high-frequency of asymmetric mode A_0 is relatively stable, which corresponds to a Rayleigh wave velocity for the case of air-medium boundary [16]. To simplify, we used the elastic wave velocity to indirectly reflect the elasticity modulus as repeated in multiple studies [17,41,42].

3. Results

3.1. Agar phantoms study

The 0.3% (n = 3), and 0.7% homogeneous agar phantoms (n = 3) were made to undergo OCE imaging. The 3D transverse elastic wave propagation can be constructed from different B-scan slices. As shown in Fig. 3, the series time instants of a 3D transient Doppler phase visualizes 3D transverse elastic wave propagation in homogeneous agar phantoms. As the air-coupled ultrasound transducer works, vibrations begin to appear on the left side of the phantoms. Over time, vibrations propagate to the right side of the phantoms. It can be found that the elastic wave propagates much faster in 0.7% homogeneous agar phantoms in Fig. 3. The elastic waves in agar phantoms are most likely to be Rayleigh waves due to the air-solid interface [16]. When we calculate the Young's modulus using shear wave formula, it's necessary to transform the Rayleigh wave velocity into shear wave velocity by applying a correction factor [16]. Considering the positive relationship between Rayleigh wave velocity and the Young's modulus, we just compared the Rayleigh wave velocity in agar phantoms rather than the Young's modulus in this study.

Based on the spatial-temporal Doppler phase images in the phantoms in Fig. 4, the elastic wave group velocity is calculated by $\Delta x / \Delta t$, which is a ratio of the distance Δx of wave propagation to the wave propagation time Δt. Considering the near field effect occurs in Figs. 4(b) and (e), the 2 mm area on the left is excluded in calculation of the elastic wave group velocity along the fast scan directions. It's also found that the elastic wave propagation direction is at an angle with the fast and slow scan directions, respectively, in Fig. 3. According to the 2D spatial-temporal Doppler phase images, the elastic wave group velocity along the fast and slow scan directions in different concentration agar phantoms was estimated as summarized in the Table 1. Based on Eq. (7), the true elastic wave group velocities in the 0.3% and 0.7% homogeneous agar phantoms were 0.77 ± 0.01 m/s and 1.82 ± 0.08 m/s, respectively.

(a)

(b)
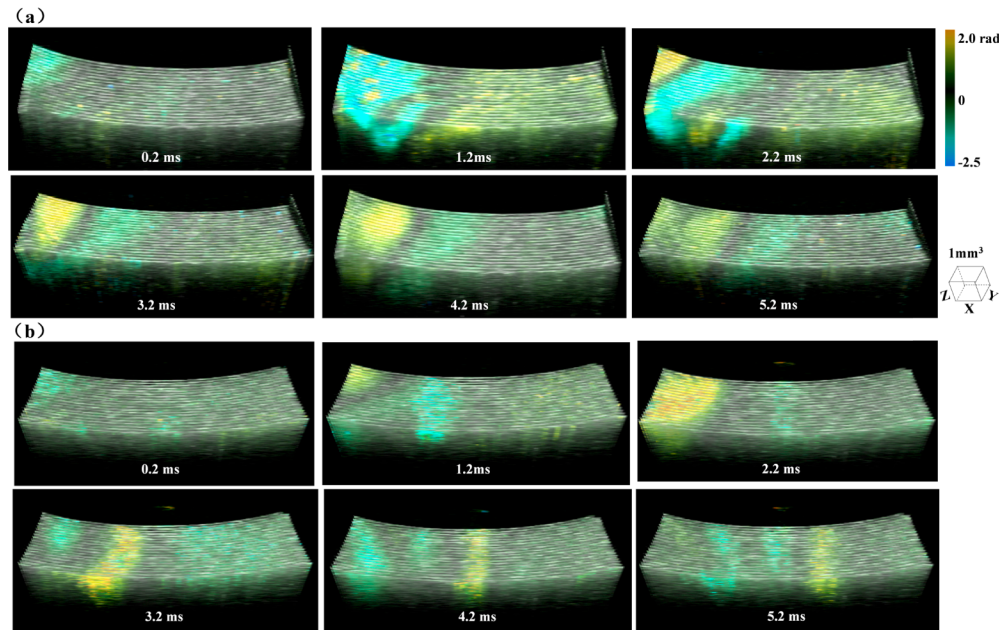
Fig. 3. 3D visualization of elastic wave propagation in the 0.3% (a) and 0.7% (b) homogeneous agar phantoms. The bottom of the right images shows the time after the excitation of the air-coupled ultrasound transducer. The series time instants of the 3D transient Doppler phase visualizes 3D transverse elastic wave propagation from left to right in homogeneous agar phantoms.

Table 1. Summary of the Elastic Wave Velocity Obtained in Different Concentrations of Agar Phantoms

| Sample	Velocity along x-axis (m/s)	Velocity along y-axis (m/s)	True velocity (m/s)
0.3% phantoms	0.90 ± 0.04	1.50 ± 0.18	0.77 ± 0.01
0.7% phantoms	1.91 ± 0.09	6.19 ± 0.16	1.82 ± 0.08

[a]Values are expressed as the mean ± standard deviation; the x-axis represents the fast scan direction while the y-axis represents the slow scan direction.

### 3.2. in-vivo healthy rabbit study

Two healthy New Zealand White rabbits (a total of four eyes) were anesthetized to undergo OCE imaging of the center cornea. Compared with the phantoms, the Doppler phase images of cornea in-vivo contained significant motion artifacts, as shown in Fig. 2. When the motion artifacts were corrected, the Doppler phase induced by the excitation of the transducer was highlighted. Corneal 2D Doppler phase images of different B-scan slices construct the 3D corneal Doppler phase images in Fig. 5 in which the series time instants present the obvious elastic wave propagation from the left side of the cornea to the right side. Layering comparison was not analyzed in this study due to no clear and uniform layering definition [17,41], and the depth-resolved Doppler phase within the cornea was averaged.

The 3D corneal spatial-temporal Doppler phase images in Fig. 6 reveal the uniform elastic wave group velocity inside the cornea. As shown in Fig. 6(b) and (c), it is found that the elastic wave velocity along the slow scan direction is much larger than that along the fast scan direction. According to Eq. (7), the true velocity was approximately equal to the velocity along the fast scan
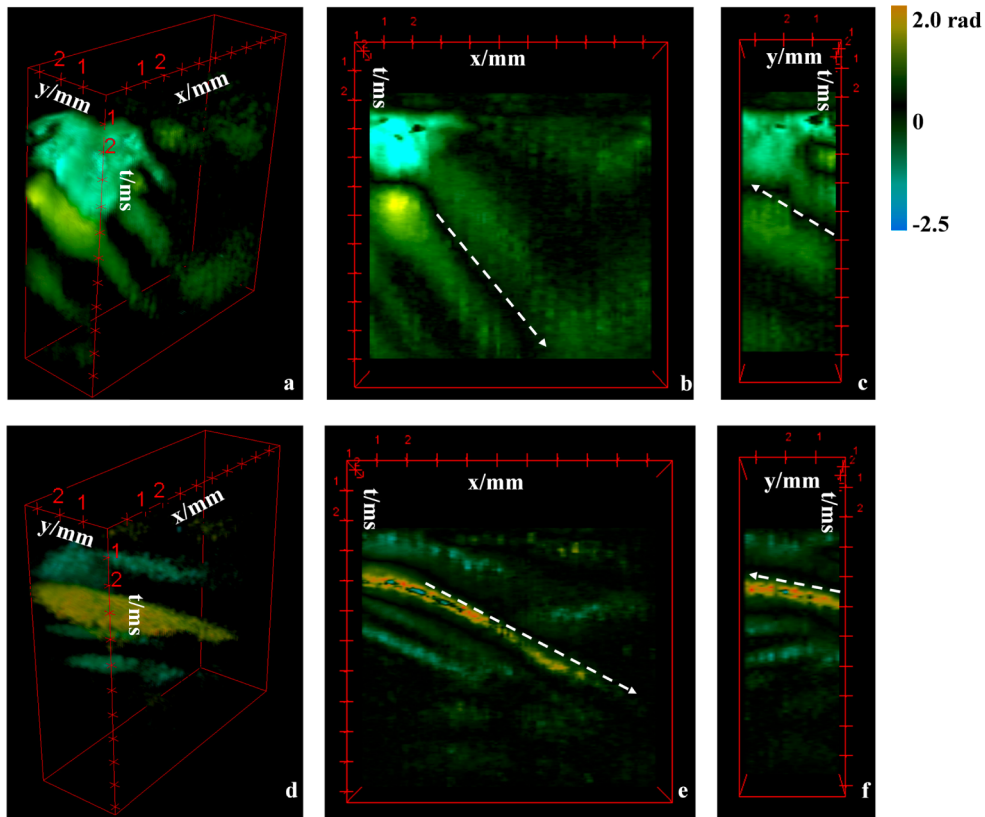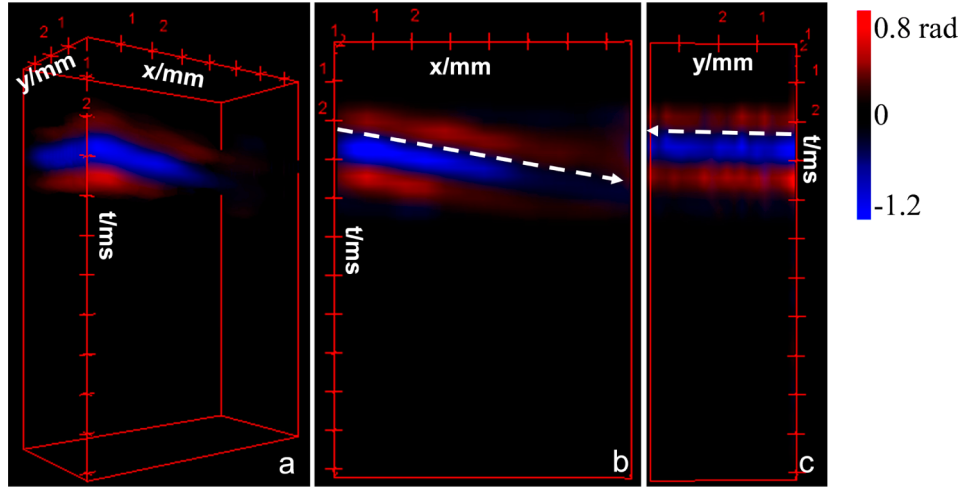
Fig. 4. Spatial-temporal Doppler phase images in the 0.3% (a-c) and 0.7% (d-f) homogeneous agar phantoms. (a, d) 3D spatial-temporal Doppler phase images; 2D spatial-temporal Doppler phase image along the fast (b, e), and slow (c, f) scan direction, respectively; (b) and (e) are profile cuts of the volume in (a) and (d) when y is ~2.0 mm. (c) and (f) are profile cuts of the volume in (a) and (d) when x is ~2.0 mm. The elastic wave velocity is calculated by the slope of the white dotted arrow.
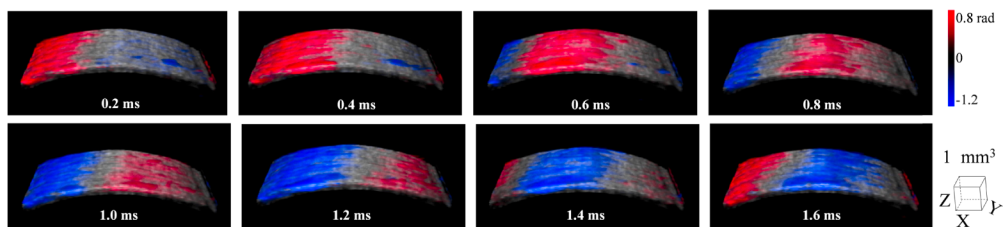
Fig. 5. 3D visualization of elastic wave propagation in the rabbit cornea in-vivo. The bottom of the right images shows the time after the excitation of the air-coupled ultrasound transducer.

direction, which suggested the corneal elastic wave traveled mainly along the fast scan direction. Therefore, we only reported the true velocity in this paper.

Fig. 6. Spatial-temporal Doppler phase images in the rabbit cornea in-vivo. (a) 3D spatial-temporal Doppler phase images; 2D spatial-temporal Doppler phase image along the fast (b) and slow (c) scan direction, respectively. The elastic wave velocity is calculated by the slope of the white dotted arrow.

Since the elastic wave mainly traveled along the fast axis in the cornea, subsequent data analysis was conducted only in this direction. The axial displacement of the cornea is related to its Doppler phase shift by using the following equation [21]:

$$D = \int_{t_1}^{t_2} \frac{\lambda_0 \Delta\phi}{4\pi n\tau} d_t, \tag{8}$$

where D is the axial displacement of the cornea, λ_0 is the center wavelength of sweep source laser, $\Delta\phi$ denotes the Doppler phase shift between two adjacent A-lines, n is the corneal refractive index, and τ is the adjacent A-line time interval.

According to the Eq. (8), the corneal spatial-temporal displacement map was obtained and transformed into the wavenumber-frequency domain by using the 2D discrete FFT. Based on the wavenumber-frequency domain map, the phase velocity of Lamb waves can be derived through Eq. (9) [43,44]:

$$C_p = \frac{\omega}{k}, \tag{9}$$

where C_p is the phase velocity, ω is the angular frequency, and k is the wavenumber. The phase velocity dispersion curve was then obtained by selecting the phase velocity with maximal intensity for corresponding frequency. As shown in Fig. 7, the phase velocity C_p of Lamb waves in the high-frequency will converge, and its value corresponds to the Rayleigh wave velocity C_R for the case of air-medium boundary. Moreover, the elastic wave main frequency f_c is the frequency at which the elastic wave energy is highest [45].

The results of four rabbit corneas are summarized in Table 2. The true elastic wave group velocity was 5.96 ± 0.55 m/s, while its Rayleigh wave velocity C_R was 7.52 ± 1.11 m/s. The coefficient of variation of three measured Rayleigh wave velocities for each rabbit cornea was 0.02-0.04.
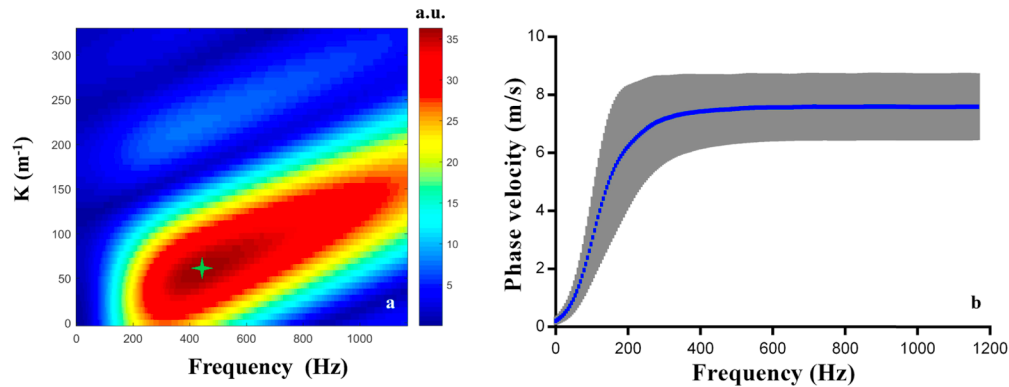
Fig. 7. Results of rabbit corneas using the Lamb wave model. (a) The wavenumber-frequency domain map. The main frequency of the elastic wave is marked as a green star. (b) The average phase velocity dispersion curve of four rabbit corneas with the standard deviation shaded regions.

Table 2. Summary of the Elastic Wave Velocity Obtained in Four Rabbit Corneas

Sample	Central corneal thickness (mm)	True group velocity (m/s)	Rayleigh wave velocity (m/s)	Main frequency (Hz)	Coefficient of variation[b]
1	348.9 ± 5.1	6.08 ± 0.23	7.66 ± 0.16	447.47 ± 17.14	0.02
2	446.6 ± 8.3	5.34 ± 0.46	6.64 ± 0.21	429.57 ± 29.69	0.03
3	390.0 ± 8.6	6.64 ± 0.24	9.04 ± 0.33	544.77 ± 20.29	0.04
4	470.8 ± 3.3	5.64 ± 0.15	6.76 ± 0.30	458.86 ± 6.76	0.04

[a]Values are expressed as the mean ± standard deviation.
[b]Coefficient of variation represents the deviation of the measured Rayleigh wave velocity.

4. Discussion and conclusion

As expected, the elasticity in different concentrations of agar phantoms showed that the elasticity was proportional to the concentrations as repeated in other studies [19,23,25], suggesting our method can quantify the elasticity of tissues. In addition, the true direction of elastic wave propagation was visualized by a series of time instants of 3D Doppler phase images, which can improve the accuracy of the elastic wave velocity, especially when non-contact excitation mechanisms, such as air-coupled ultrasound and air-puff, are used [38].

We assessed the elasticity of rabbit corneas in-vivo by OCE using air-coupled ultrasound. Compared with phantoms, there are significant axial motion artifacts in the corneas in-vivo. The corneal displacement induced by the air-coupled ultrasound is smaller than the axial motion so that it is buried by motion artifacts. Therefore, it's necessary to correct the motion artifacts and extract the corneal vibration. There are two basic ways to address the motion artifacts: namely, hardware-based methods and software-based methods [36]. Hardware-based methods use additional hardware mounted onto the OCT system to avoid motion artifacts during the imaging while software-based methods try to correct motion artifacts retrospectively using OCT data processing. One of the hardware-based methods is increasing the imaging speed of the OCT system to freeze out motion during OCT acquisition [46]. However, the typical imaging speed of commercially available systems is less than 200 kHz, which cannot avoid motion artifacts completely using a 3D OCE scan mode. Considering that only axial motion artifacts of the cornea exists after general anesthesia, software-based methods seem more simple and effective than other hardware-based methods like tracking OCT or a combination of OCT with additional

imaging modalities [36]. We used the consecutive data correlation algorithm to distinguish corneal vibration from motion artifacts in our study. The eye motion is relatively still during a short time window while the corneal vibration is propagating because the velocity of the elastic wave inside the cornea is larger than the eye motion. As expected, the Doppler phase images visualized the elastic wave propagation clearly after the axial motion artifacts correction. As shown in Fig. 2, parameter T has an effect on the correction effect of the algorithm on axial motion artifacts. In this study, the in-vivo corneal elasticity from the previous literatures was used to calculate the range of the T value. Then the T value within its range was selected and optimized to correct the axial motion artifacts. However, if we do not know the elastic properties of the sample in advance, we have to search for the appropriate T value within a larger range. Although this process is time-consuming, it does not affect the measured elastic wave velocity.

Although there are reported studies using an elastic wave model to measure the group velocity of in-vivo corneas in mouse and swine animal model [23,47–49], there are no reports of in-vivo rabbit cornea elastography studies using Lamb wave or elastic wave model based on OCT and ultrasound. Previous studies indicate that the group velocity has a positive relationship with the phase velocity of Lamb waves in the high-frequency of asymmetric mode A_0 [50]. Thus, the group velocity is selected to ensure the comparability of the results with other literatures. Several studies have reported the elastic wave velocity of swine corneas in-vivo is 5.1-9.8 m/s while that of mouse corneas is 5.0-7.2 m/s [23,47–49]. Although corneal stiffness is affected by species, their values are not significantly different, which is similar to our experimental results. Urs *et al.* measured in-vivo rabbit cornea elasticity using static displacement methods with an ultrasound imaging system [51]. We converted their results into elastic wave velocity and found it is smaller than our measured velocity, which may be caused by imaging principles, IOP, CCT, and other factors [17,18,48,49]. In addition, it's found that the elastic wave velocity in corneas in-vivo is larger than ex-vivo as mentioned in other studies [41,42]. Rabbit eyes ex-vivo are often preserved in 0.9% saline solution hypotonic to the corneal stroma, which causes slight corneal swelling [18]. Under physiological conditions, the corneal epithelial and endothelium have the function of preventing corneal edema, so as to keep the cornea transparent [1,52]. In this work, although the cornea is dropped with normal saline solution, the corneal epithelial and endothelial cells of living rabbits can make the cornea in a physiological state. The cornea is reported to soften as it hydrates, which may explain why our results are larger than those of the previous in vitro samples [18]. Moreover, the IOP in ex-vivo corneas is much lower than in-vivo conditions, causing the elastic wave velocity to decrease [17,48,49]. Precise knowledge of corneal biomechanics is critical for early diagnosis, optimal management of diseased corneas (e.g., keratoconus), and predicting the risks of surgical intervention of healthy corneas, such as post-LASIK [3–8]. In addition, traditional IOP measurements are often affected by corneal stiffness [9]. Our study demonstrates that 3D OCE using air-coupled ultrasound is feasible to measure corneal elasticity in-vivo. With the advantage of non-invasive, air-coupled ultrasound, OCE can reduce the discomfort of patients and repeat measurements of corneal elasticity in clinical practice.

A major limitation of this study is the 3D OCE acquisition time, which is about 30 s. After general anesthesia, the main motion artifacts of rabbit cornea in-vivo are axial motion artifacts but not the transverse movement. In clinical practice, if the acquisition time is too long, it will increase the risk of transverse eye movement which adds to the difficulty of correcting the motion artifacts [36]. There are several methods to solve the above issue [36]. Firstly, a visual target is set in the OCE system to stabilize the subjects' fixed vision, thus reducing the occurrence of the eye lateral voluntary motion. Secondly, increasing the sampling rate of the image systems can also reduce the occurrence of eye lateral motion [46]. Finally, tracking OCT can effectively compensate for the deviation in the scan position that is caused by the eye lateral motion and, therefore, can remove motion artifacts [53].

In summary, we have used air-coupled ultrasound OCE to visualize 3D elastic wave propagation of the cornea in-vivo with an axial motion artifacts correction algorithm to provide a robust assessment of corneal elasticity. Air-coupled ultrasound OCE shows promise in becoming a routine tool to measure corneal elasticity in clinical practice.

Disclosures

Dr. Zhongping Chen has a financial interest in OCT Medical Inc., which, however, did not support this work.

References

1. D. W. DelMonte and T. Kim, "Anatomy and physiology of the cornea," J. Cataract Refractive Surg. **37**(3), 588–598 (2011).
2. J. Ma, Y. Wang, P. Wei, and V. Jhanji, "Biomechanics and structure of the cornea: implications and association with corneal disorders," Surv. Ophthalmol. **63**(6), 851–861 (2018).
3. C. J. Roberts and W. J. Dupps Jr, "Biomechanics of corneal ectasia and biomechanical treatments," J. Cataract Refractive Surg. **40**(6), 991–998 (2014).
4. A. Murueta-Goyena and P. Canadas, "Visual outcomes and management after corneal refractive surgery: A review," Journal of Optometry **11**(2), 121–129 (2018).
5. M. Moshirfar, J. C. Albarracin, J. D. Desautels, O. C. Birdsong, S. H. Linn, and P. C. Hoopes, "Ectasia following small-incision lenticule extraction (SMILE): a review of the literature," Clin. Ophthalmol. **11**, 1683–1688 (2017).
6. G. Wollensak, E. Spoerl, and T. Seller, "Riboflavin/ultraviolet-a–induced collagen crosslinking for the treatment of keratoconus," Am. J. Ophthalmol. **135**(5), 620–627 (2003).
7. F. Raiskup-Wolf, A. Hoyer, E. Spoerl, and L. E. Pillunat, "Collagen crosslinking with riboflavin and ultraviolet-A light in keratoconus: long-term results," J. Cataract Refractive Surg. **34**(5), 796–801 (2008).
8. H. Hashemi, M. Miraftab, M. A. Seyedian, F. Hafezi, H. Bahrmandy, S. Heidarian, K. Amanzadeh, H. Nikbin, A. Fotouhi, and S. Asgari, "Long-term Results of an Accelerated Corneal Cross-linking Protocol (18 mW/c2) for the Treatment of Progressive Keratoconus," Am. J. Ophthalmol. **160**(6), 1164–1170.e1 (2015).
9. S. McCafferty, G. Lim, W. Duncan, E. Enikov, and J. Schwiegerling, "Goldmann Tonometer Prism with an Optimized Error Correcting Applanation Surface," Trans. Vis. Sci. Tech. **5**(5), 4–5 (2016).
10. J. Shin, T. W. Kim, S. J. Park, M. Yoon, and J. W. Lee, "Changes in biomechanical properties of the cornea and intraocular pressure after myopic laser in situ keratomileusis using a femtosecond laser for flap creation determined using ocular response analyzer and Goldmann applanation tonometry," J. Glaucoma **24**(3), 195–201 (2015).
11. R. Sihota, D. Angmo, D. Ramaswamy, and T. Dada, "Simplifying "target" intraocular pressure for different stages of primary open-angle glaucoma and primary angle-closure glaucoma," Indian J. Ophthalmol. **66**(4), 495–505 (2018).
12. K. J. Parker, M. M. Doyley, and D. J. Rubens, "Corrigendum: Imaging the elastic properties of tissue: the 20 year perspective," Phys. Med. Biol. **57**(16), 5359–5360 (2012).
13. S. Wang and K. V. Larin, "Optical coherence elastography for tissue characterization: a review," J. Biophotonics. **8**(4), 279–302 (2015).
14. J. Zhu, L. Qi, Y. Miao, T. Ma, C. Dai, Y. Qu, Y. He, Y. Gao, Q. Zhou, and Z. Chen, "3D mapping of elastic modulus using shear wave optical micro-elastography," Sci. Rep. **6**(1), 35499 (2016).

15. D. P. Pinero and N. Alcon, "Corneal biomechanics: a review," Clin. Exp. Optom. **98**(2), 107–116 (2015).
16. M. A. Kirby, I. Pelivanov, S. Song, L. Ambrozinski, S. J. Yoon, L. Gao, D. Li, T. T. Shen, R. K. Wang, and M. O'Donnell, "Optical coherence elastography in ophthalmology," J. Biomed. Opt. **22**(12), 1–28 (2017).
17. L. Ambrozinski, S. Song, S. J. Yoon, I. Pelivanov, D. Li, L. Gao, T. T. Shen, R. K. Wang, and M. O'Donnell, "Acoustic micro-tapping for non-contact 4D imaging of tissue elasticity," Sci. Rep. **6**(1), 38967 (2016).
18. M. Singh, Z. Han, J. Li, S. Vantipalli, S. R. Aglyamov, M. D. Twa, and K. V. Larin, "Quantifying the effects of hydration on corneal stiffness with noncontact optical coherence elastography," J. Cataract Refractive Surg. **44**(8), 1023–1031 (2018).
19. J. Zhu, J. Yu, Y. Qu, Y. He, Y. Li, Q. Yang, T. Huo, X. He, and Z. Chen, "Coaxial excitation longitudinal shear wave measurement for quantitative elasticity assessment using phase-resolved optical coherence elastography," Opt. Lett. **43**(10), 2388–2391 (2018).
20. C. Sun, B. Standish, and V. X. Yang, "Optical coherence elastography: current status and future applications," J. Biomed. Opt. **16**(4), 043001 (2011).
21. W. Qi, R. Chen, L. Chou, G. Liu, J. Zhang, Q. Zhou, and Z. Chen, "Phase-resolved acoustic radiation force optical coherence elastography," J. Biomed. Opt. **17**(11), 110505 (2012).
22. J. Zhang, B. Rao, L. Yu, and Z. Chen, "High-dynamic-range quantitative phase imaging with spectral domain phase microscopy," Opt. Lett. **34**(21), 3442–3444 (2009).
23. J. Li, S. Wang, R. K. Manapuram, M. Singh, F. M. Menodiado, S. Aglyamov, S. Emelianov, M. D. Twa, and K. V. Larin, "Dynamic optical coherence tomography measurements of elastic wave propagation in tissue-mimicking phantoms and mouse cornea in-vivo," J. Biomed. Opt. **18**(12), 121503 (2013).
24. J. Li, S. Wang, M. Singh, S. Aglyamov, S. Emelianov, M. D. Twa, and K. V. Larin, "Air-pulse OCE for assessment of age-related changes in mouse cornea in-vivo," Laser Phys. Lett. **11**(6), 065601 (2014).
25. S. Wang, K. V. Larin, J. Li, S. Vantipalli, R. K. Manapuram, S. Aglyamov, S. Emelianov, and M. Twa, "A focused air-pulse system for optical-coherence-tomography-based measurements of tissue elasticity," Laser Phys. Lett. **10**(7), 075605 (2013).
26. L. Ambrozinski, I. Pelivanov, S. Song, S. J. Yoon, D. Li, L. Gao, T. T. Shen, R. K. Wang, and M. O'Donnell, "Air-coupled acoustic radiation force for non-contact generation of broadband mechanical waves in soft media," Appl. Phys. Lett. **109**(4), 043701 (2016).
27. Y. Qu, Y. He, A. Saidi, Y. Xin, Y. Zhou, J. Zhu, T. Ma, R. H. Silverman, D. S. Minckler, Q. Zhou, and Z. Chen, "in-vivo Elasticity Mapping of Posterior Ocular Layers Using Acoustic Radiation Force Optical Coherence Elastography," Invest. Ophthalmol. Visual Sci. **59**(1), 455–461 (2018).
28. J. Zhu, Y. Qu, T. Ma, R. Li, Y. Du, S. Huang, K. K. Shung, Q. Zhou, and Z. Chen, "Imaging and characterizing shear wave and shear modulus under orthogonal acoustic radiation force excitation using OCT Doppler variance method," Opt. Lett. **40**(9), 2099–2102 (2015).
29. S. Moon and Z. Chen, "Phase-stability optimization of swept-source optical coherence tomography," Biomed. Opt. Express **9**(11), 5280–5295 (2018).
30. T. E. Gomez Alvarez-Arenas, "Acoustic impedance matching of piezoelectric transducers to the air," IEEE Trans. Ultrason. Ferroelectr. Freq. Control **51**(5), 624–633 (2004).
31. T. E. Gomez Alvarez-Arenas, J. Camacho, and C. Fritsch, "Passive focusing techniques for piezoelectric air-coupled ultrasonic transducers," Ultrasonics **67**, 85–93 (2016).
32. S. P. Kelly, G. Hayward, and T. E. Alvarez-Arenas, "Characterization and assessment of an integrated matching layer for air-coupled ultrasonic applications," IEEE Trans. Ultrason. Ferroelectr. Freq. Control **51**(10), 1314–1323 (2004).
33. T. G. Alvarez-Arenas and L. Diez, "Ultrasonic Single Element and Sectorized Array Transducers with Omnidirectional 2D Field Distribution for Non-Contact Human-Machine Interface and Echo-Location," Elektron. Elektrotech. **23**(4), 51–55 (2017).
34. R. de Kinkelder, J. Kalkman, D. J. Faber, O. Schraa, P. H. Kok, F. D. Verbraak, and T. G. van Leeuwen, "Heartbeat-induced axial motion artifacts in optical coherence tomography measurements of the retina," Invest. Ophthalmol. Visual Sci. **52**(6), 3908–3913 (2011).
35. G. Nair, M. Kim, T. Nagaoka, D. E. Olson, P. M. Thule, M. T. Pardue, and T. Q. Duong, "Effects of common anesthetics on eye movement and electroretinogram," Doc. Ophthalmol. **122**(3), 163–176 (2011).
36. A. Baghaie, Z. Yu, and R. M. D'Souza, "Involuntary eye motion correction in retinal optical coherence tomography: Hardware or software solution?" Med. Image Anal. **37**, 129–145 (2017).
37. M. Singh, J. Li, Z. Han, S. Vantipalli, C. H. Liu, C. Wu, R. Raghunathan, S. R. Aglyamov, M. D. Twa, and K. V. Larin, "Evaluating the Effects of Riboflavin/UV-A and Rose-Bengal/Green Light Cross-Linking of the Rabbit Cornea by Noncontact Optical Coherence Elastography," Invest. Ophthalmol. Visual Sci. **57**(9), OCT112 (2016).
38. P. Song, A. Manduca, H. Zhao, M. W. Urban, J. F. Greenleaf, and S. Chen, "Fast shear compounding using robust 2-D shear wave speed calculation and multi-directional filtering," Ultrasound Med. Biol. **40**(6), 1343–1355 (2014).
39. Z. Han, S. R. Aglyamov, J. Li, M. Singh, S. Wang, S. Vantipalli, C. Wu, C. h. Liu, M. D. Twa, and K. V. Larin, "Quantitative assessment of corneal viscoelasticity using optical coherence elastography and a modified Rayleigh-Lamb equation," J. Biomed. Opt. **20**(2), 020501 (2015).
40. Z. Han, J. Li, M. Singh, C. Wu, C. H. Liu, R. Raghunathan, S. R. Aglyamov, S. Vantipalli, M. D. Twa, and K. V. Larin, "Optical coherence elastography assessment of corneal viscoelasticity with a modified Rayleigh-Lamb wave model," J. Mech. Behav. Biomed. Mater. **66**, 87–94 (2017).

41. S. Wang and K. V. Larin, "Noncontact depth-resolved micro-scale optical coherence elastography of the cornea," Biomed. Opt. Express **5**(11), 3807–3821 (2014).
42. S. Wang and K. V. Larin, "Shear wave imaging optical coherence tomography (SWI-OCT) for ocular tissue biomechanics," Opt. Lett. **39**(1), 41–44 (2014).
43. K. Zhou, N. Le, Z. Huang, and C. Li, "High-intensity-focused ultrasound and phase-sensitive optical coherence tomography for high resolution surface acoustic wave elastography," J. Biophotonics **11**(2), e201700051 (2018).
44. K. Zhou, C. Li, S. Chen, G. Nabi, and Z. Huang, "Feasibility study of using the dispersion of surface acoustic wave impulse for viscoelasticity characterization in tissue mimicking phantoms," J. Biophotonics **12**(1), e201800177 (2019).
45. A. C. Carolina, S. Chen, W. U. Matthew, and F. G. James, "Acoustic Radiation Force Induced Creep-Recovery (ARFICR) A non-invasive method to characterize tissue viscoelasticity," IEEE Trans. Ultrason. Ferroelectr. Freq. Control **65**(1), 3–13 (2018).
46. B. Potsaid, I. Gorczynska, V. J. Srinivasan, Y. Chen, J. Jiang, A. Cable, and J. G. Fujimoto, "Ultrahigh speed Spectral / Fourier domain OCT ophthalmic imaging at 70,000 to 312,500 axial scans per second," Opt. Express **16**(19), 15149–15169 (2008).
47. J. A. Izatt, J. G. Fujimoto, V. V. Tuchin, S. Song, Z. Huang, T.-M. Nguyen, E. Y. Wong, B. Arnal, M. O'Donnell, and R. K. Wang, "Shear wave elastography using phase sensitive optical coherence tomography," Proc. SPIE **8934**, 89340U (2014).
48. T. M. Nguyen, J. F. Aubry, D. Touboul, M. Fink, J. L. Gennisson, J. Bercoff, and M. Tanter, "Monitoring of cornea elastic properties changes during UV-A/riboflavin-induced corneal collagen cross-linking using supersonic shear wave imaging: a pilot study," Invest. Ophthalmol. Visual Sci. **53**(9), 5948–5954 (2012).
49. T. M. Nguyen, J. F. Aubry, M. Fink, J. Bercoff, and M. Tanter, "in-vivo evidence of porcine cornea anisotropy using supersonic shear wave imaging," Invest. Ophthalmol. Visual Sci. **55**(11), 7545–7552 (2014).
50. I. Pelivanov, L. Gao, J. Pitre, M. A. Kirby, S. Song, D. Li, T. T. Shen, R. K. Wang, and M. O'Donnell, "Does group velocity always reflect elastic modulus in shear wave elastography?" J. Biomed. Opt. **24**(07), 1 (2019).
51. R. Urs, H. O. Lloyd, and R. H. Silverman, "Acoustic radiation force for noninvasive evaluation of corneal biomechanical changes induced by cross-linking therapy," J. Med. Ultrasound **33**(8), 1417–1426 (2014).
52. D. H. Geroski, M. Matsuda, R. W. Yee, and H. F. Edelhauser, "Pump Function of the Human Corneal Endothelium: Effects of Age and Cornea Guttata," Ophthalmology **92**(6), 759–763 (1985).
53. R. D. Ferguson, D. X. Hammer, L. A. Paunescu, S. Beaton, and J. S. Schuman, "Tracking optical coherence tomography," Opt. Lett. **29**(18), 2139–2141 (2004).